GaAs/Al0.8Ga0.2As separate absorption and multiplication region x-ray spectroscopic avalanche photodiodes

Article (Accepted Version)

$GaAs/Al_{0.8}Ga_{0.2}As$ Separate Absorption and Multiplication Region X-ray Spectroscopic Avalanche Photodiodes

M.D.C. Whitaker[1*], G. Lioliou[1], A.B. Krysa[2], and A.M. Barnett[1]

[1]*Space Research Group, Sch. of Engineering and Informatics, University of Sussex, Falmer, Brighton, BN1 9QT, UK*

[2]*National Epitaxy Facility, University of Sheffield, Mappin Street, Sheffield, S1 3JD, UK*

A $GaAs/Al_{0.8}Ga_{0.2}As$ Separate Absorption and Multiplication (SAM) X-ray avalanche photodiode (APD) structure was grown by metalorganic vapour phase epitaxy. Mesa photodiodes of different diameter (200 µm and 400 µm) were fabricated from the structure. Two of the photodiodes (one of each diameter) were characterised at 20 °C for their electrical properties and response to X-rays using an ^{55}Fe radioisotope X-ray (Mn Kα = 5.9 keV; Mn Kβ = 6.49 keV) source. An energy resolution of 508 eV ± 5 eV Full Width at Half Maximum (FWHM) at 5.9 keV was achieved at an apparent avalanche gain, *M*, of 1.1. This is the best energy resolution so far reported for $GaAs/Al_xGa_{1-x}As$ X-ray SAM APDs. The noise components associated with the achievable spectroscopic energy resolutions are reported. Comparisons between the 200 µm and 400 µm diameter $GaAs/Al_xGa_{1-x}As$ SAM X-ray APDs and recently studied GaAs p^+-i-n^+ detectors were made, showing that the inclusion of the avalanche layer improves the achievable energy resolution; energy resolutions of 508 eV FWHM at 5.9 keV at M = 1.1 and 603 eV FWHM at 5.9 keV at M = 1.2 were achieved with the 200 µm and 400 µm diameter $GaAs/Al_xGa_{1-x}As$ SAM X-ray APDs respectively; this is better than was previously reported for similar devices without avalanche layers: 690 eV FWHM at 5.9 keV and 730 eV FWHM at 5.9 keV for 200 µm and 400 µm diameter GaAs p^+-i-n^+ detectors respectively (G.Lioliou et al., J. Appl. Phys. 122, 244506 (2017)).

KEYWORDS

GaAs; AlGaAs; SAM; APD; X-ray detector; Spectroscopy

I. INTRODUCTION

Due to the limitations of narrow bandgap (typically Si) X-ray spectrometers commonly in use today [1, 2], a variety of wide bandgap materials, such as GaAs [3-7], diamond [8, 9], SiC [10-12], $In_{0.5}Ga_{0.5}P$ [13, 14], $Al_{0.52}In_{0.48}P$ [15-17], and $Al_xGa_{1-x}As$ [18-21], have been investigated as potential X-ray detector replacements. The cooling systems and radiation shielding often required for Si X-ray spectrometers [22] place substantial burdens on spacecraft mass, volume, and power consumption, limiting their suitability for certain space science applications (e.g. missions to study the surface of Mercury, or the Jovian moons, where temperatures and/or radiation intensities are significant). Wide bandgap materials, such as GaAs and $Al_xGa_{1-x}As$, offer an alternative. Such materials can operate in a large range of thermal and radiation environments, while still providing sub-keV spectral resolutions at soft X-ray energies [22]. In the case of GaAs, its wider bandgap (1.43 eV for GaAs cf. 1.12 eV for Si [22]), larger X-ray absorption coefficient (837 cm^{-1} for GaAs cf. 346 cm^{-1} for Si, at 5.9 keV [23]), and improved radiation hardness in comparison to Si [24], allows for superior energy resolutions at high temperature [25], thinner X-ray detecting structures [26], and potentially longer instrument lifetimes in intense radiation environments.

*Corresponding author, E-mail address: M.Whitaker@sussex.ac.uk

Various prototype GaAs based X-ray spectrometers have been reported, with most work focused on GaAs p^+-i-n^+ mesa X-ray photodiodes operated in the non-avalanche regime. Circular mesa GaAs, 200 µm diameter, 7 µm thick i layer, p^+-i-n^+ photodiodes have been characterised across the temperature range 60 °C to 0 °C, with an energy resolution of 750 eV FWHM at 5.9 keV for the best performing device at 20 °C [6]. Similar GaAs photodiodes (10 µm i layer) have been characterised over the temperature range 100 °C to -20 °C, with an energy resolution of 690 eV FWHM at 5.9 keV reported at room temperature (20 °C) [27]. GaAs planar p^+-i-n^+ photodiode arrays have also been reported with very promising results; a 5 × 5 pixel, 40 µm i layer, GaAs p^+-i-n^+ diode array structure had a reported energy resolution of 266 eV FWHM at 5.9 keV at room temperature [3]. GaAs arrays of a similar structure, but with thicker epilayer layers (325 µm i layer), had a reported energy resolution of 300 eV FWHM at 5.9 keV at room temperature [28].

$Al_xGa_{1-x}As$, due to the material's ability to be tailored to particular application environments by adjusting the Al fraction (e.g. a reduction in Al fraction reduces the bandgap), has gained attention as an interesting material for X-ray detection [21, 26, 29]. Most work has focused on $Al_xGa_{1-x}As$ p^+-i-n^+ mesa photodiodes, operated within the non-avalanche regime. Circular mesa $Al_{0.8}Ga_{0.2}As$, 200 µm diameter, 1 µm i layer, p^+-i-n^+ photodiodes have been characterised across the temperature range 90 °C to -30°C, with an energy resolution of 1.07 keV FWHM at 5.9 keV reported at 20 °C [29]. Circular mesa $Al_{0.2}Ga_{0.8}As$, 200 µm diameter, 3 µm i layer, p^+-i-n^+ photodiodes have been characterised across the temperature range 20 °C to -20 °C, with an energy resolution of 1.06 keV FWHM at 5.9 keV reported at 20 °C [21]. A 2 × 2 square pixel $Al_{0.2}Ga_{0.8}As$ array (each photodiode area 200 µm by 200 µm, 3 µm i layer) was also recently reported with improved results; an energy resolution of 760 eV FWHM at 5.9 keV at 20 °C was achieved [26].

Whilst non-avalanche GaAs and $Al_xGa_{1-x}As$ X-ray detectors show great promise, the demands they place on their preamplifier electronics are more stringent than those of narrower bandgap materials like Si, because the electron-hole pair creation energies of GaAs and $Al_xGa_{1-x}As$ are larger (e.g. 4.2 eV for GaAs cf. 3.6 eV for Si [22]). Avalanche photodiodes (APDs) potentially reduce those demands by increasing the amount of charge created from the absorption of an X-ray photon. However, the greater operating biases required can cause higher leakage currents which results in more parallel white noise.

APDs are widely used in photonic detection systems, most notably within telecommunications [30-33], to improve response relative to that of conventional p^+-i-n^+ photodiodes [30]. The increased response from such APDs is due to the impact ionisation process, where charge carriers gain enough kinetic energy to generate electron-hole pairs during collisions with atoms in the lattice [34, 35].

For photons of infrared to ultraviolet wavelength, where the photon energy is of the same order as the bandgap energy of the detector material, the stochastic nature of the impact ionisation process in APDs commonly adds noises (quantified by the so called the excess noise factor, N_x) to the signal [36, 37] such that

$$N_x = kM + \left(2 - \frac{1}{M}\right)(1 - k), \quad (1)$$

where k (= β/α) is the ratio between the hole (β) and electron (α) ionisation coefficients, which represent the inverse of the mean distance between successive impact ionisation events [36]. In most compound semiconductors, k can range from 0.3 to 1.0, leading to a large N_x [38]. Hence, as per Eq. 1, assuming an extension of applicability of this model to the X-ray case, a poor energy resolution was originally expected [38]. For this reason, it was originally thought that the use of APDs would degrade the resolution of X-ray spectrometers and hence they were not extensively investigated [39]. However, recent studies have improved the understanding of APDs [31, 35, 36, 38, 40]. Notably, Tan et al. [38] showed that the common model of excess noise is not directly applicable at X-ray energies, since the distribution of avalanche gains tightens as the initiating photon energy, E, is increased, thus leading to significantly lower additional noise for X-rays than would be expected in the case for infrared, visible, or UV photons [38]. Additional design choices such as using very thin avalanche layers can also be used to reduce excess noise [31].

The first X-ray APDs were complex staircase band structures [18, 41, 42]. For example, a GaAs/$Al_xGa_{1-x}As$ SAM APD (320 µm × 450 µm active area) was reported to function as an X-ray detector at room temperature, utilising a series of staircase multiplication regions [18]; an energy resolution of 900 eV FWHM at 13.96 keV was reported at an avalanche multiplication of 4.1 at room temperature [18]. More recent work has concentrated on simpler SAM APD structures [43]. For example, a thin (430 nm GaAs absorption layer, 220 nm $Al_{0.8}Ga_{0.2}As$ multiplication layer) GaAs/$Al_{0.8}Ga_{0.2}As$ SAM X-ray APD was reported at room temperature [44]; it had an energy resolution of 1.08 keV FWHM at 5.9 keV, at an avalanche multiplication of 3.5.

In this work we report the growth, fabrication, and characterisation at room temperature (20 °C) of two new circular GaAs/$Al_{0.8}Ga_{0.2}As$ SAM X-ray photodiodes of different diameter (200 µm and 400 µm). The results are compared with recently reported non-avalanche GaAs p^+-i-n^+ X-ray photodiodes of the same size (200 µm and 400 µm diameter) and with the same absorption layer thickness (10 µm) [27]. The same measurement techniques and readout electronics were used in both cases. The work shows that the addition of the avalanche layer improves the energy resolution. This unambiguous comparison of the detectors both with and without an avalanche layer but otherwise of the same design provides conclusive evidence that the addition of an avalanche layer can be used to improve the energy resolution of a spectroscopic photon counting X-ray detector.

II. DIODE DESIGN

The GaAs/$Al_{0.8}Ga_{0.2}As$ SAM structure (see Fig. 1) was grown by metalorganic vapour phase epitaxy upon a commercial GaAs n^+ substrate. The photodiode layer details are outlined in Table 1. Circular mesa structures of 200 µm diameter and 400 µm diameter were etched using a 1:1:1 H_3PO_4:H_2O_2:H_2O solution followed by 10 s in a 1:8:80 H_2SO_4:H_2O_2:H_2O solution. Ohmic contacts consisting of 200 nm Au and 20 nm Ti were evaporated upon the top p^+ side of the mesa structures and ohmic contacts consisting of 200 nm Au and 20 nm InGe were evaporated upon the back side of the substrate. The top contacts covered 45% of the 200 µm diameter diode's face and 33% of the 400 µm diameter diode's face.

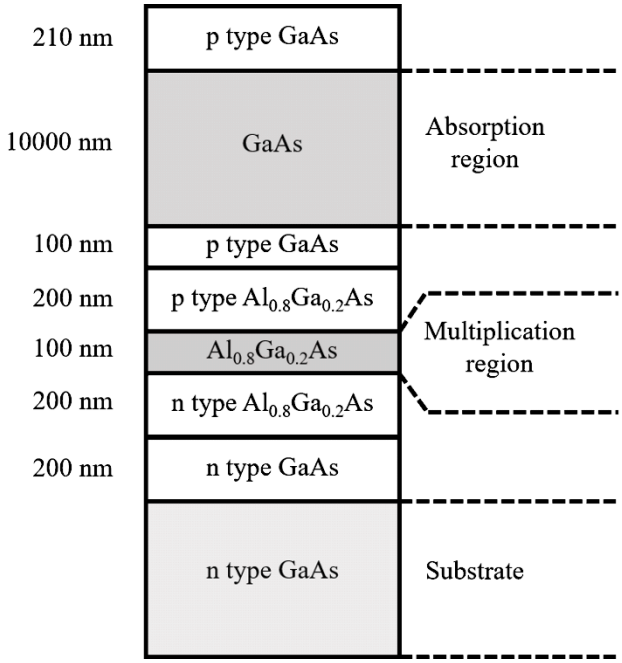

Fig. 1. Schematic of GaAs/$Al_{0.8}Ga_{0.2}As$ SAM structure.

Table 1. GaAs/$Al_{0.8}Ga_{0.2}As$ SAM layer details.

Material	Dopant	Dopant type	Thickness (nm)	Doping density (cm^{-3})
GaAs	Zn	p	10	1×10^{19}
GaAs	Zn	p	200	2×10^{18}
GaAs			10000	Undoped
GaAs	Zn	p	100	2×10^{17}
$Al_{0.8}Ga_{0.2}As$	Zn	p	200	2×10^{17}
$Al_{0.8}Ga_{0.2}As$			100	Undoped
$Al_{0.8}Ga_{0.2}As$	Si	n	200	2×10^{18}
GaAs	Si	n	200	2×10^{18}
GaAs n^+ substrate				

III. DETECTOR ELECTRICAL CHARACTERISATION

A. Capacitance as a function of applied reverse bias

For each GaAs/$Al_{0.8}Ga_{0.2}As$ SAM photodiode (200 µm and 400 µm diameter), capacitance as a function of reverse bias, V_R, was measured using an HP 4275A LCR Meter (50 mV rms signal magnitude; 1 MHz frequency). A Keithley 6487 voltage source/picoammeter was used to bias the detectors. Each device was placed within a custom-made, light-tight, electromagnetically screened test fixture and, for temperature control, inserted in a TAS Micro MT environmental chamber. An appropriately positioned thermocouple was used to ensure thermal equilibrium (20 °C) was reached between the environmental chamber and the devices. The test fixture and environmental chamber were purged with dry N_2 (<5% relative humidity) in order to remove any humidity related effects [6]. The environmental chamber was set to 20 °C and left for 1 hour before measuring to ensure thermal

equilibrium. The measured capacitances as functions of reverse bias for (a) the 200 µm diameter device and (b) the 400 µm diameter device is shown in Fig. 2.

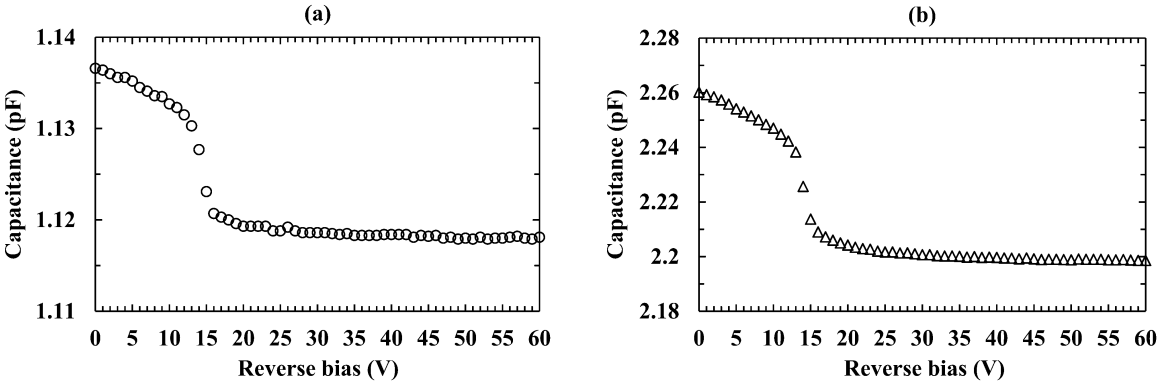

Fig. 2. Capacitance for (a) the 200 µm diameter device and (b) the 400 µm diameter device, as a function of applied reverse bias, at 20 °C. The empty package capacitance, in each case, has not been subtracted.

The measured capacitance of both packaged devices decreased with increasing reverse bias, from 1.14 pF and 2.26 pF at $V_R = 0$ V for the 200 µm and 400 µm diameter device respectively, to 1.12 pF and 2.20 pF at $V_R = 60$ V for the 200 µm and 400 µm diameter device respectively. The uncertainty associated with each individual capacitance measurement was ≈ ± 0.03 pF. However, because a set of measurements were taken without modifying the conditions (e.g. no variations in electrical connections and temperature), fittings on the experimental data provide a more appropriate uncertainty for relative changes [45]. Exponential fittings on the measured capacitance for each device were performed as a function of reverse bias. An uncertainty of ± 0.4 fF was estimated. The drop in capacitance across both the 200 µm and 400 µm diameter devices, within the range $13 \text{ V} \leq V_R \leq 16$ V, indicated that the punch-through voltage (the voltage at which the multiplication region rapidly depletes) was ≈ 14 V [44].

The measured capacitance, C_M, included both the diode capacitance, C_D, and the package capacitance, C_P, since the devices were packaged. C_P was removed by assuming a constant capacitance density as a function of device area. The capacitance density of the 200 µm diameter device and the 400 µm diameter device at each applied reverse bias were compared, and the empty package capacitance calculated. A mean average empty package capacitance (0.76 pF) was calculated for C_P and was subsequently subtracted from C_M for each device. Fig. 3 presents the capacitance densities for the 200 µm and 400 µm diameter devices.

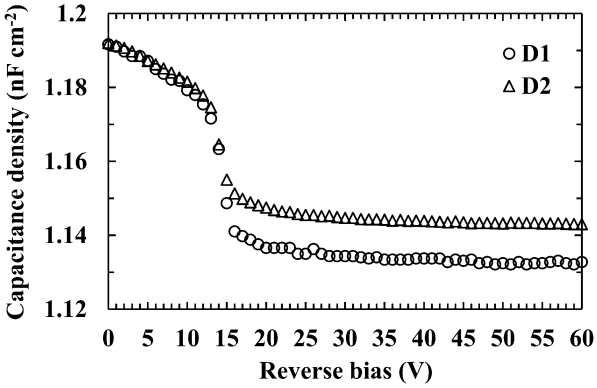

Fig. 3. Capacitance density for the 400 µm diameter device (triangles) and the 200 µm diameter device (circles) as a function of applied reverse bias, at 20 °C, taking into account the empty package capacitance (0.76 pF).

The capacitances of the devices were defined primarily by the depletion layer capacitance, C_{DL} of each device [34]. Therefore, the depletion width, W, could be calculated using the equation

$$W = \frac{\varepsilon_0 \varepsilon A}{C_{DL}}, \quad (2)$$

where A is the device area, ε is the relative permittivity of the material, and ε_0 is the permittivity of free space [34]. For the reported devices, multiple materials (GaAs and $Al_{0.8}Ga_{0.2}As$) influence C_{DL}, with their associated contributions difficult to detangle. As such, in order to calculate W, the devices were approximated to be simple GaAs structures (ε = 13.16 [46]). Since ε of $Al_{0.8}Ga_{0.2}As$ (= 10.628 [47]) is smaller in value, the presently reported W should be taken as an upper limit. The Debye length of GaAs (0.06 µm) was also taken into account when calculating the depletion width uncertainty [48]. Fig. 4 (a) shows the depletion width as a function of applied reverse bias.

The depletion width increased as a function of applied reverse bias for both devices, increasing from 9.8 µm ± 0.1 µm at V_R = 0 V for the 200 µm and 400 µm diameter device, to 10.3 µm ± 0.1 µm and 10.2 µm ± 0.1 µm at V_R = 60 V for the 200 µm and 400 µm diameter device, respectively. As was the case in Fig. 2, the increase in depletion width across both the 200 µm and 400 µm diameter devices, between 13 V and 16 V, indicated the punch-through voltage. Linear least squares fitting was applied to both devices, and indicated that the devices were fully depleted at $V_R \geq 50$ V.

The GaAs/$Al_{0.8}Ga_{0.2}As$ SAM APD structure quantum detection efficiency was calculated using the Beer-Lambert law, assuming that the active region was solely confined to the GaAs absorption layer and that it was fully depleted and active. The results can be seen in Fig. 4 (b). For photons of 5.9 keV energy, the quantum detection efficiencies of the devices structure presented here were 0.56 in areas not covered by the top contact, and 0.46 in areas covered by the top contact. The weighted quantum efficiency assuming uniform illumination of the devices was 0.52 and 0.53 for the 200 µm and 400 µm diameter detectors, respectively.

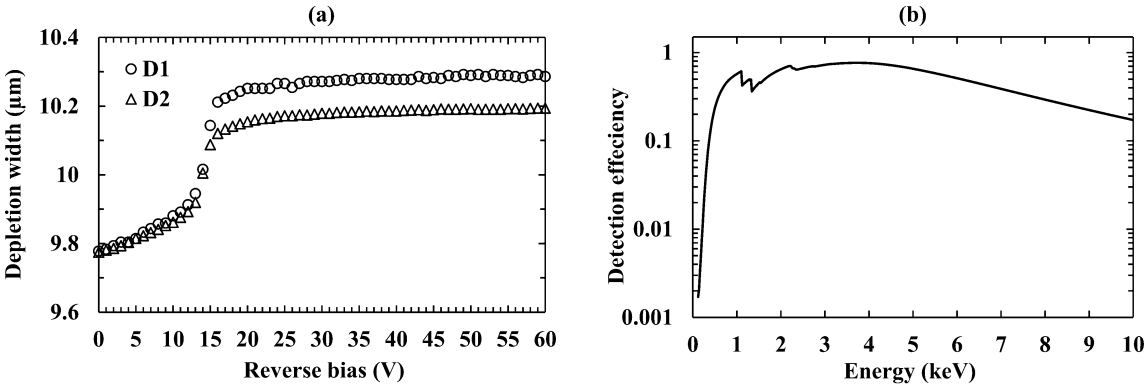

Fig. 4. (a) Calculated depletion width for the 200 μm diameter device (circles) and the 400 μm diameter device (triangles) as a function of applied reverse bias, at 20 °C. (b) Calculated detection efficiency for the GaAs/$Al_{0.8}Ga_{0.2}As$ SAM APD structure as a function of energy. The Al K, Ga L, and As L X-ray absorption edges are responsible for the detection efficiency discontinuities.

The general nonuniform distributions equation [34] was used to calculate the carrier concentration of the space charge region, *N*, where,

$$\frac{\mathrm{d}(1/C_{DL}^{\,2})}{\mathrm{d}V_R} = \frac{2}{\mathrm{q}\varepsilon_0\varepsilon N}, \tag{3}$$

where q is the elementary charge and the other symbols have previously been defined. For both devices, at a calculated depletion width ≈ 10 μm, the carrier concentration reached a minimum of ≈ 7×10^{14} cm^{-3}. Fig. 5 presents the carrier concentration for the GaAs/$Al_{0.8}Ga_{0.2}As$ detectors as a function of calculated depletion width. Variation in the apparent carrier concentration between the 200 μm and 400 μm devices was within the uncertainty of the measurements.

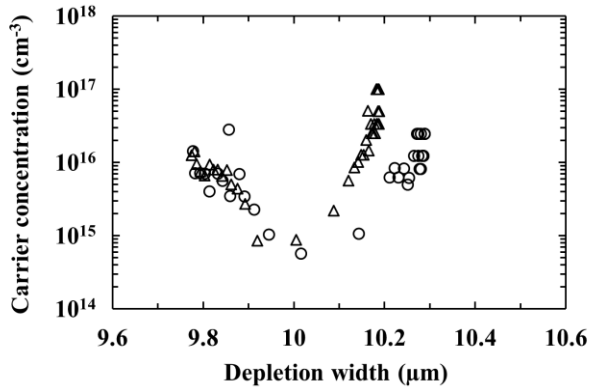

Fig. 5. Carrier concentration for the 200 μm (circles) and 400 μm (triangles) diameter devices as a function of calculated depletion width.

B. Current as a function of applied reverse bias

The leakage current of the 200 μm and 400 μm diameter devices was measured using a Keithley 6487 voltage source/picoammeter as a function of applied reverse bias. The environmental conditions were the same as for the

capacitance measurements. Fig. 6 presents the measured leakage current, I_R, of the packaged devices as a function of applied reverse bias.

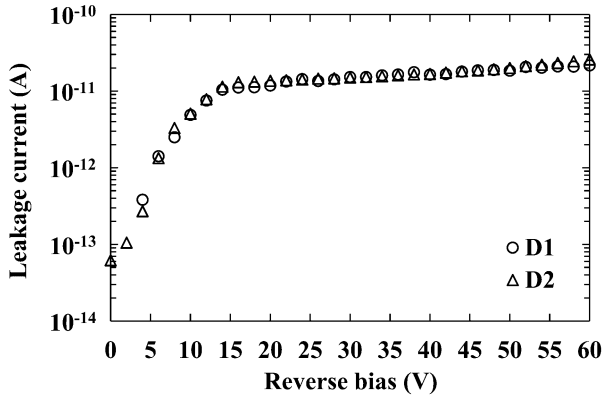

Fig. 6. Leakage current for the 200 µm diameter device (circles) and the 400 µm diameter device (triangles) as a function of applied reverse bias.

For both packaged devices, the leakage current increased with increasing reverse bias. At the maximum applied reverse bias (60 V), the leakage currents were measured to be 21.6 pA ± 0.8 pA for the 200 µm device and 25.7 pA ± 0.5 pA for the 400 µm device. The uncertainties associated with the current measurements were dominated by the uncertainty associated with a single measurement from the Keithley 6487 voltage source/picoammeter.

In order to determine the corresponding leakage current density, J_R, of the devices, the leakage current associated with the package (and measurement system) was determined by measuring an empty package of identical type. It was found that the empty package's leakage current was smaller than the uncertainty (± 0.4 pA) of the instrument, it was therefore considered negligible. The apparent leakage current density, as shown in Fig. 7, of the 400 µm diameter device was improved (lower) relative to the 200 µm diameter device (20.4 nA cm^{-2} ± 0.4 nA cm^{-2} for the 400 µm diameter device cf. 68.8 nA cm^{-2} ± 2.7 nA cm^{-2} for the 200 µm diameter device, at the maximum applied reverse bias (60 V). This suggested that the leakage current did not scale with junction area. The presence of a non-negligible surface leakage current, possibly due to the devices being unpassivated [49, 50], cannot be excluded entirely, but the measured leakage currents do not scale with circumference either. A similar trend was recently reported for GaAs p^+-i-n^+ mesa X-ray photodiodes of the same size (200 µm and 400 µm diameter) and with the same absorption layer thickness (10 µm) [27]. For the present devices, the difference in leakage current density with junction area was possibly attributable to damage caused by wirebonding to the thin metal contacts, resulting in a dominating additional leakage current component.

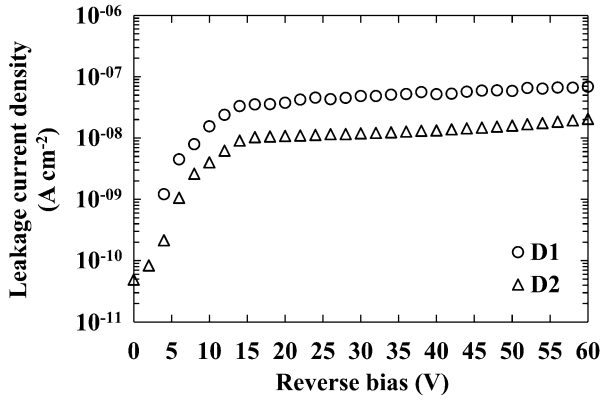

Fig. 7. Apparent leakage current density for the 200 µm (circles) and 400 µm (triangles) diameter devices as a function of applied reverse bias, at 20 °C.

The leakage current densities of the presently reported devices were greater than those measured for recently reported GaAs p^+-i-n^+ mesa X-ray photodiodes [27]. At an internal electric field strength, E_f, of 50 kV cm^{-1} (corresponding to 51 V applied reverse bias for the GaAs/$Al_{0.8}Ga_{0.2}As$ devices, assuming E_f was uniform and across only the depleted region), leakage current densities of 61.8 nA cm^{-2} ± 1.5 nA cm^{-2} and 16.4 nA cm^{-2} ± 0.4 nA cm^{-2} were measured for the 200 µm diameter and 400 µm diameter devices respectively. At the same E_f, leakage current densities of 15 nA cm^{-2} and 6 nA cm^{-2} were measured for the 200 µm and 400 µm GaAs devices respectively, at 20 °C [27].

IV. PHOTON COUNTING X-RAY SPECTROSCOPY

A. Experimental measurements and determination of the spectrometers' energy resolutions

In order to characterise the X-ray detection performance of the GaAs/$Al_{0.8}Ga_{0.2}As$ SAM APD devices, each detector was connected, in turn, to a custom-made low-noise charge-sensitive feedback-resistorless preamplifier, similar in design to ref. [51]. The preamplifier, in each case, was connected to a shaping amplifier (Ortec 572A) and a multi-channel analyser (Ortec Easy-MCA 8k). An ^{55}Fe X-ray (Mn Kα = 5.9 keV; Mn Kβ = 6.49 keV) source (≈ 131 MBq) was positioned ≈ 4 mm above each GaAs/$Al_{0.8}Ga_{0.2}As$ SAM APD in turn. The resulting spectrometers: S_{200} (using the 200 µm diameter detector) and S_{400} (using the 400 µm diameter detector) were installed within a TAS Micro MT environmental chamber for temperature control. The environmental chamber temperature was set to 20 °C, and allowed to stabilise for 1 hour before measurements were taken. A thermocouple was positioned close to the spectrometer such that temperature equilibrium between the environmental chamber and the spectrometer could be monitored. The environmental chamber was purged continually throughout the measurements with dry N_2 (< 5% relative humidity) as to reduce any humidity related effects [52].

Spectra were accumulated for each spectrometer as a function of detector applied reverse bias. The applied reverse bias was initially set to 0 V, then increased in 1 V steps up to 50 V. The reverse bias was increased further in steps of 5 V, up to 60 V. After each voltage change, the system was allowed to stabilise for 5 minutes before taking a measurement. Since the two detectors had different active areas, the live time limits of each spectrum were set differently: spectra accumulated with S_{200} had a live time limit of 100 s; spectra accumulated with S_{400}

had a live time limit of 25 s. A shaping time of 0.5 µs was used; this was the best available shaping time for each system. The accumulated ^{55}Fe spectra for the 200 µm and 400 µm diameter GaAs/$Al_{0.8}Ga_{0.2}As$ SAM APD spectrometers can be seen in Fig. 8.

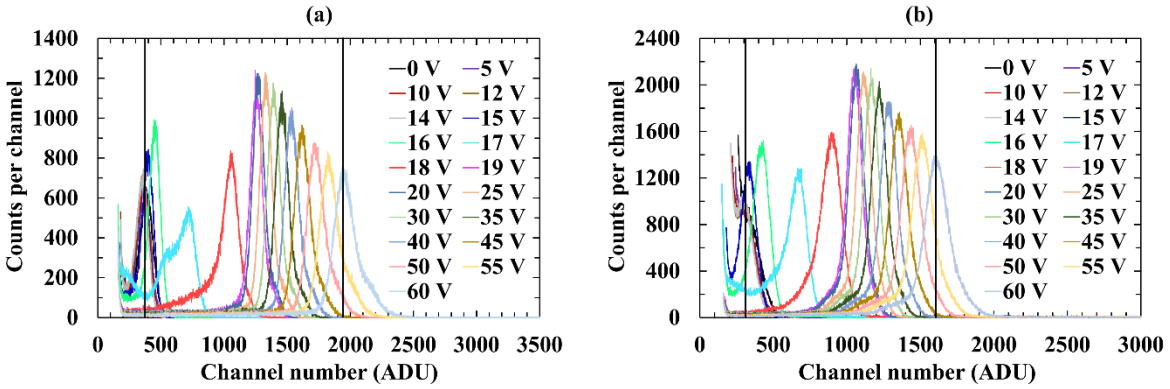

Fig. 8. Accumulated ^{55}Fe spectra using the spectrometers (a) S_{200} and (b) S_{400}. The same shaping time (0.5 µs) and temperature (20 ºC) were used for all spectra. The vertical black lines indicate the positions of the combined 5.9 keV (Mn Kα) and 6.49 keV (Mn Kβ) X-ray photopeaks from the ^{55}Fe X-ray source accumulated with the detectors reverse biased at 0 V and 60 V.

For each accumulated spectrum from the ^{55}Fe X-ray (Mn Kα = 5.9 keV; Mn Kβ = 6.49 keV) source, Gaussian fitting was applied. The relative emission ratio [53] and the relative detection efficiency of the GaAs/$Al_{0.8}Ga_{0.2}As$ SAM APDs at these energies were taken into account in fitting the Mn Kα and Kβ peaks. The Mn Kα and Kβ peaks were not individually resolved by the spectrometer; as such, the peak detected is the combination of the Mn Kα and Kβ lines. The form of spectroscopic response was consistent with a SAM APD; this was further exemplified by plotting the change in 5.9 keV peak centroid position (corrected for changes in zero energy noise peak position and plotted in terms of the MCA's analogue to digital units, ADU, scale) as a function of applied detector reverse bias, as shown in Fig. 9.

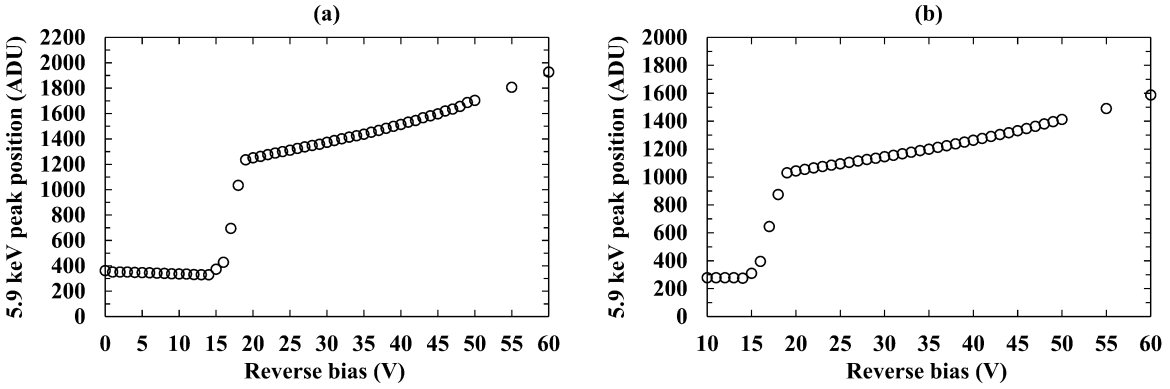

Fig. 9. Difference, in ADU, between the 0 keV position and the position of the centroid of the fitted 5.9 keV peak as a function of applied detector reverse bias, at a shaping time of 0.5 µs, and a temperature of 20 ºC for the spectrometers (a) S_{200} and (b) S_{400}.

The sharp increase in 5.9 keV peak position between 14 V and 19 V for both the 200 µm and 400 µm diameter devices, as shown in Fig. 9, was attributed to an improved charge collection efficiency from reaching the

punch-through voltage (see Fig. 2). At applied detector reverse biases less than the punch-through voltage, charge carriers cannot readily travel through the $Al_{0.8}Ga_{0.2}As$ junction (see Table 1) [18], limiting the charge collection efficiency. The increasing 5.9 keV peak position as a function of applied detector bias beyond 19 V was a result of increases in avalanche multiplication. The apparent multiplication factor, *M*, was calculated for both spectrometers by calculating the ratio between the fitted 5.9 keV peak position at each bias and the fitted 5.9 keV peak position at unity gain ($M = 1$) and complete charge collection, assumed to be achieved at $V_R = 19$ V applied to the detector. The apparent multiplication factor as a function of applied detector reverse bias can be seen in Fig. 10.

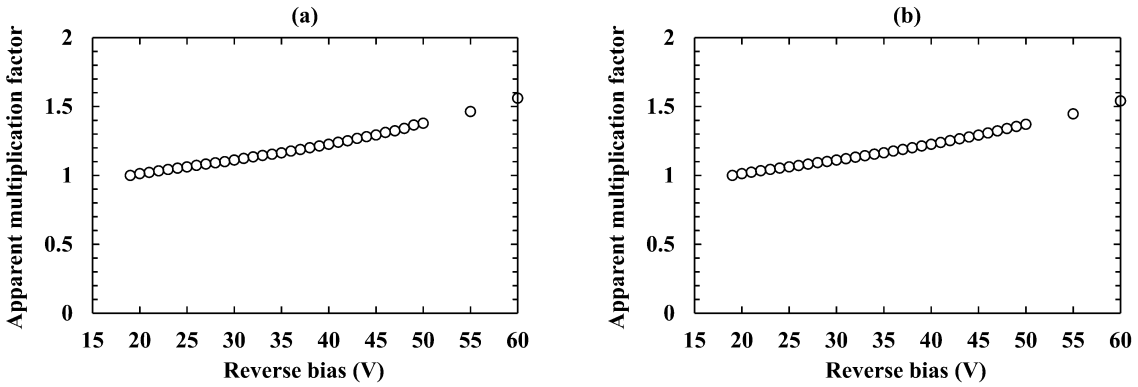

Fig. 10. Apparent multiplication factor of the 5.9 keV ^{55}Fe photopeak as a function of applied detector reverse bias for the spectrometers (a) S_{200} and (b) S_{400}, at 20 ºC. Unity gain was set to 19 V.

The spectra were energy calibrated by assuming a linear variation of output charge with energy and using the positions of the so called zero energy noise peak and fitted 5.9 keV peak. The energy resolution (FWHM at 5.9 keV) was then calculated for each accumulated spectrum. Fig. 11 presents the energy resolution of each spectrometer as a function of applied detector reverse bias.

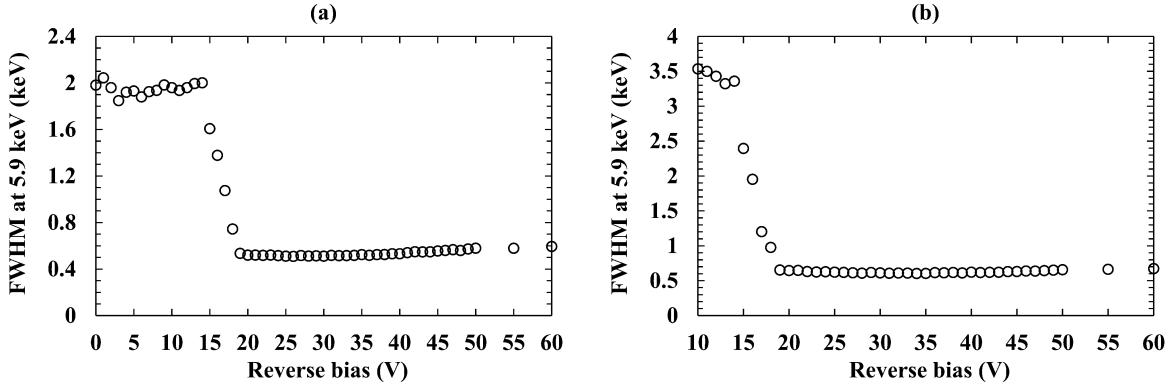

Fig. 11. FWHM at 5.9 keV for the spectrometers (a) S_{200} and (b) S_{400} as a function of applied detector reverse bias at a shaping time of 0.5 µs, and at 20 ºC.

The improved charge collection efficiency, due to overcoming the punch-through voltage of the detectors, resulted in an abrupt improvement in energy resolution (FWHM at 5.9 keV) of the spectroscopic systems around the punch through voltage, as shown in Fig. 11. At $V_R = 14$ V, the FWHM at 5.9 keV was 2.00 keV ± 0.05 keV and 3.36 keV

± 0.05 keV for the spectrometers S_{200} and S_{400}, respectively. At V_R = 19 V, the FWHM at 5.9 keV was 534 eV ± 5 eV and 653 eV ± 6 eV for S_{200} and S_{400}, respectively. The best measured energy resolution for the spectrometer S_{200} was 508 eV ± 5 eV, achieved at V_R = 26 V, corresponding to an apparent multiplication factor of 1.1. The best measured energy resolution for the spectrometer S_{400} was 603 eV ± 6 eV, achieved at V_R = 34 V, corresponding to an apparent multiplication factor of 1.2. ^{55}Fe X-ray spectra accumulated with the spectrometers S_{200} and S_{400} can be seen in Fig. 12 and Fig. 13 respectively.

Both the 200 µm diameter and 400 µm diameter GaAs/$Al_{0.8}Ga_{0.2}As$ SAM APD devices reported here, had improved performance relative to the recently studied GaAs p^+-i-n^+ photodiodes [27]. At 20 ºC, energy resolutions of 690 eV and 730 eV FWHM at 5.9 keV were reported for the 200 µm and 400 µm GaAs p^+-i-n^+ photodiode, respectively [27]. The presently reported spectrometers also had improved performance compared to the previously reported GaAs/$Al_{0.8}Ga_{0.2}As$ SAM APD spectrometers which had a FWHM at 5.9 keV = 1.08 keV at an avalanche gain of M = 3.5 at room temperature [44].

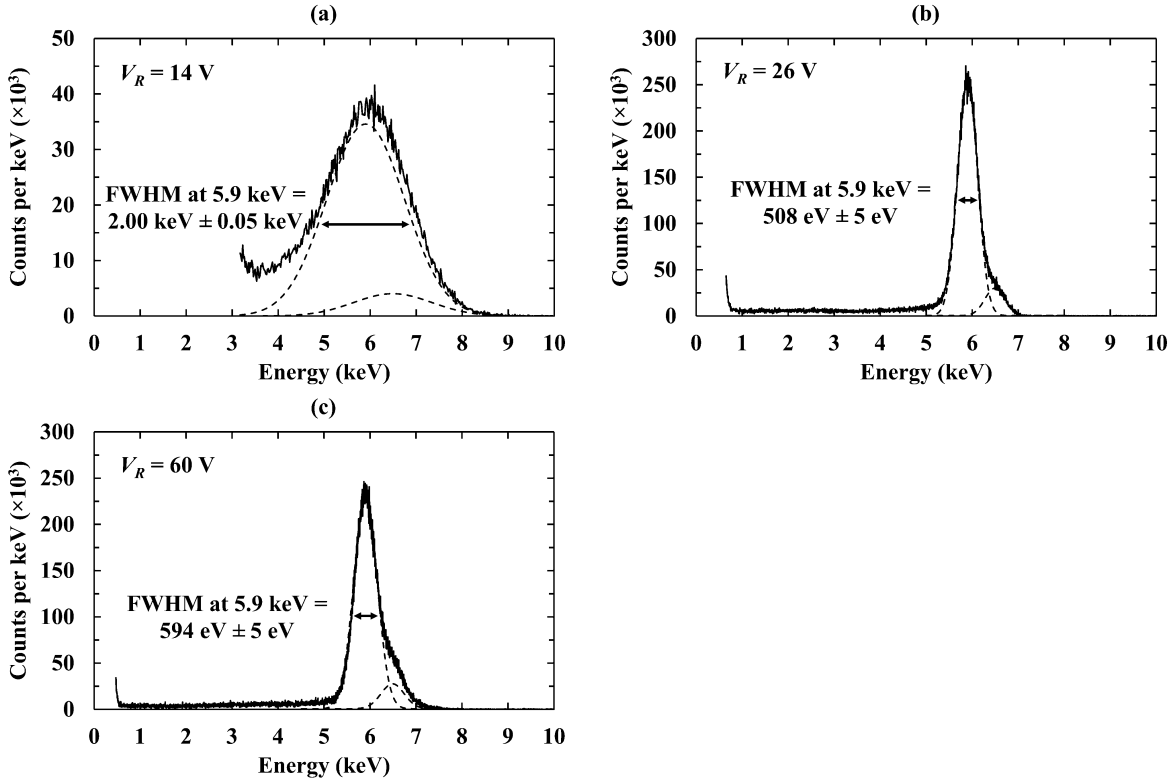

Fig. 12. ^{55}Fe X-ray spectra accumulated with the 200 µm diameter detector based spectrometer, at 20 °C, a shaping time of 0.5 µs, and a reverse bias of (a) 14 V, (b) 26 V, and (c) 60 V. The fitted 5.9 keV (Mn Kα) and 6.49 keV (Mn Kβ) peaks have been plotted (dashed lines). The accumulated spectra have been normalised into counts per keV in order to account for the differing channel widths.

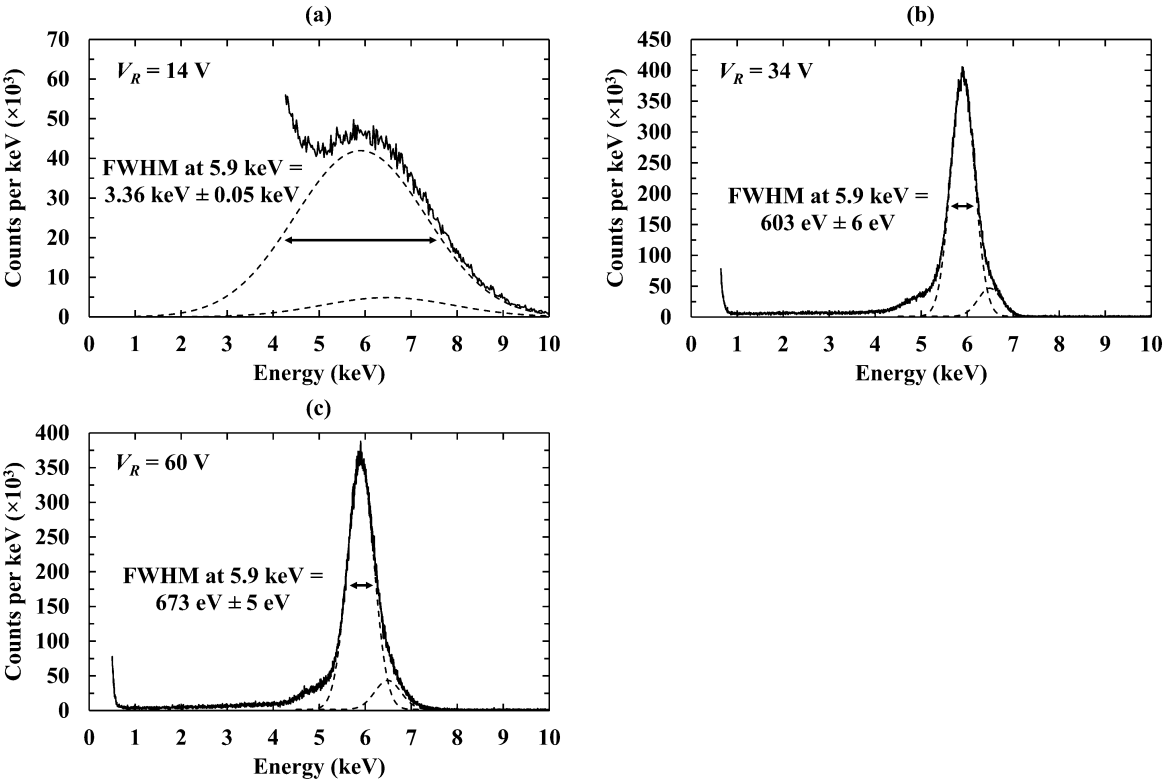

Fig. 13. ^{55}Fe X-ray spectra accumulated with the 400 µm diameter detector based spectrometer, at 20 °C, a shaping time of 0.5 µs, and a reverse bias of (a) 14 V, (b) 34 V, (c) and 60 V. The fitted 5.9 keV (Mn Kα) and 6.49 keV (Mn Kβ) peaks have been plotted (dashed lines). The accumulated spectra have been normalised into counts per keV in order to account for the differing channel widths.

B. Origin of the secondary peak in the obtained X-ray spectra

As could be seen in Fig. 13, at sufficiently high applied detector biases ($V_R \geq 17$ V), a small secondary peak appears to the left (low energy) side of the fitted peaks. The secondary peak appears as a shoulder on the main combined peak as they are not resolved from each other. This secondary peak arises as a consequence of the GaAs layer not having a 100 % absorption efficiency for the X-ray photons (see Fig. 4b); some photons are transmitted through the GaAs layer and absorbed in the $Al_{0.8}Ga_{0.2}As$ layers. This can be proven by consideration of the electron-hole pair creation energies of each material.

Due to the difference in electron-hole pair creation energy of GaAs (ω_{GaAs} = 4.19 eV ± 0.03 eV at 20 °C [54]) and $Al_{0.8}Ga_{0.2}As$ (ω_{AlGaAs} = 5.07 eV ± 0.08 eV at 20 °C [55]), the average number of charge carriers generated in each material by the absorption of a photon of energy, E, also differs.

The ratio of the average numbers of charge carriers (N_{AlGaAs} for $Al_{0.8}Ga_{0.2}As$ and N_{GaAs} for GaAs) created by the absorption of a photon of energy, E, in conjunction with the known electron-hole pair creation energy of GaAs, can be used to determine ω_{AlGaAs}, where

$$\omega_{AlGaAs} = \omega_{GaAs}\left(\frac{N_{GaAs}}{N_{AlGaAs}}\right). \quad (4)$$

The primary and secondary peak of the spectra obtained with S_{400}, with the detector biased at 34 V and 60 V respectively, were fitted with Gaussians for the ^{55}Fe 5.9 keV (Mn Kα) and 6.49 keV (Mn Kβ) peak emissions in the accepted ratio [53], see Fig. 14; the relative detection efficiencies of the Mn Kα and Mn Kβ photons were also taken into account [49]. The accepted value of ω_{GaAs} was then used in conjunction with Eq. 4 to calculate ω_{AlGaAs}. With the detector biased at 34 V and 60 V, ω_{AlGaAs} was found to be 5.04 eV ± 0.08 eV and 5.06 eV ± 0.08 eV respectively, which are in agreement with the accepted value (ω_{AlGaAs} = 5.07 eV ± 0.08 eV at 20 °C [55]). Thus, it was demonstrated that the secondary, left shoulder, peak arises as a consequence of X-ray absorption in the $Al_{0.8}Ga_{0.2}As$ layers by computation of the electron-hole pair creation energy of $Al_{0.8}Ga_{0.2}As$ from the spectra.

The secondary peak, clearly visible as a shoulder in Fig. 13 and Fig. 14 (400 µm diameter detector), was less visible in Fig. 12 (200 µm diameter detector). This was attributed to the size difference between the two investigated detectors, where the front face of the 400 µm diameter detector received four times more photons than the 200 µm diameter detector.

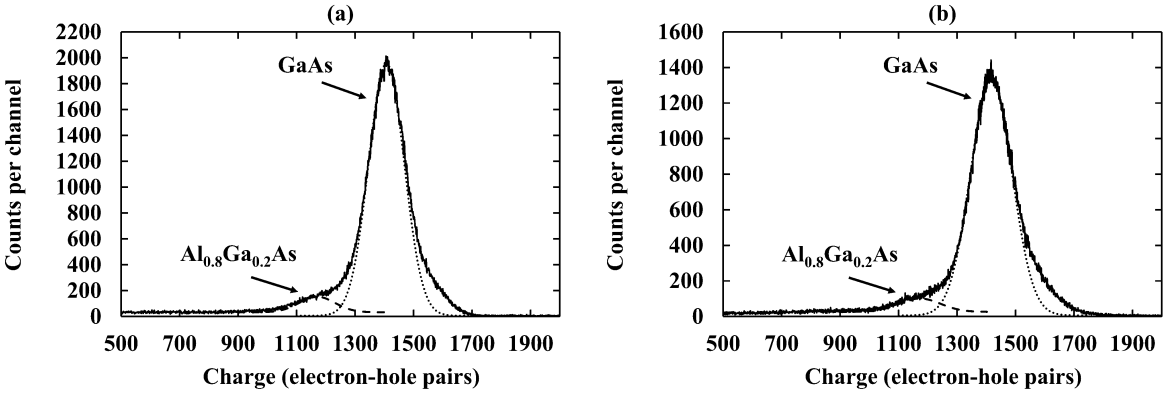

Fig. 14. ^{55}Fe X-ray spectra accumulated with S_{400} at a reverse bias of (a) 34 V, and (b) 60 V. Charge calibration was achieved using the positions of the zero energy noise peak of the preamplifier and the GaAs peak, together with the accepted ω_{GaAs} value. The dashed and dotted lines are the fitted 5.9 keV (Mn Kα) peaks for the $Al_{0.8}Ga_{0.2}As$ and GaAs materials respectively; the 6.49 keV Mn Kβ peaks were considered and included in the analysis but are not shown in the figures for clarity

C. Noise analysis

Four sources of noise influence the energy resolution of a charge-sensitive preamplifier coupled to a semiconductor detector operating in avalanche mode, these are: the Fano noise, N_F [56]; incomplete charge collection noise, R [22]; the electronic noise, A [57]; and the excess noise factor, N_x [44].

The Fano noise, assuming that X-ray photons incident on the reported detectors are absorbed only within the GaAs absorption region, can be calculated using the equation

$$N_F = 2.355\omega_{GaAs}\sqrt{FE/\omega_{GaAs}}, \quad (5)$$

where F (0.12 [58]) is the Fano factor of GaAs and the other symbols have previously been defined. N_F was calculated to be 13 e^- rms at 5.9 keV (128 eV FWHM at 5.9 keV) for the GaAs/$Al_{0.8}Ga_{0.2}As$ SAM APD. Since

the calculated Fano noise was less than the reported spectrometers measured energy resolution, other noise contributions were clearly affecting the spectroscopic system.

The electronic noise from the detector and preamplifier of a photodiode X-ray spectrometer consists of dielectric noise, N_D, series white noise (including the induced gate drain current noise), N_{SW}, parallel white noise, N_{PW}, and $1/f$ series noise, $N_{1/f}$ [19]. Dielectric noise is induced by lossy dielectrics close to the input of the spectrometer (e.g. the packaging of the preamplifier input Junction Field-Effect Transistor (JFET) and detector) [59]. Series white noise is caused by capacitances at the input of the spectrometer (e.g. the input JFET (JFET capacitance = 2 pF [60]) and the detector (see Fig. 2)) [27]. Parallel white noise is induced by leakage currents from the input JFET (JFET leakage current = 1 pA [60]) and the detector (see Fig. 6) [27]. For a review of the various noise components, the reader is directed to refs [59, 61, 62].

The dielectric noise, series white noise, parallel white noise, and $1/f$ series noise contributions were calculated for each spectrometer (S_{200} and S_{400}) via the standard methods for semiconductor X-ray devices connected to charge-sensitive preamplifiers [59]. The results can be seen in Fig. 15. It should be noted that, in the case of the dielectric noise contributions, only a lower bound value could be calculated directly; whilst dielectric noise from the JFET, feedback capacitor, and GaAs/$Al_{0.8}Ga_{0.2}As$ SAM APD device could be estimated [19, 25], additional lossy dielectrics close to the preamplifier input could have also contributed to the noise. Similarly, due to the prototype nature of the preamplifier, the presence of unknown capacitances may have also added to the series white noise contribution. The dielectric noise and series white noise were thus considered in two parts: known noise contributions and stray noise contributions. Subtracting the expected Fano noise and the electronic noise contributions ($1/f$ noise, parallel white noise, known series white noise (including induced gate drain current noise), and known dielectric noise) from the measured FWHM in quadrature, yields a combination of stray series white noise, stray dielectric noise, incomplete charge collection noise, excess noise, and possibly stray parallel white noise contributions (so called the remaining noise contribution). Changes in detector capacitance were included in the known series white noise and known dielectric noise calculations, whilst the JFET was considered to contribute a constant capacitance (2 pF [60]) to both calculations. A constant JFET leakage current (1 pA [60]) was included in the known parallel white noise calculation.

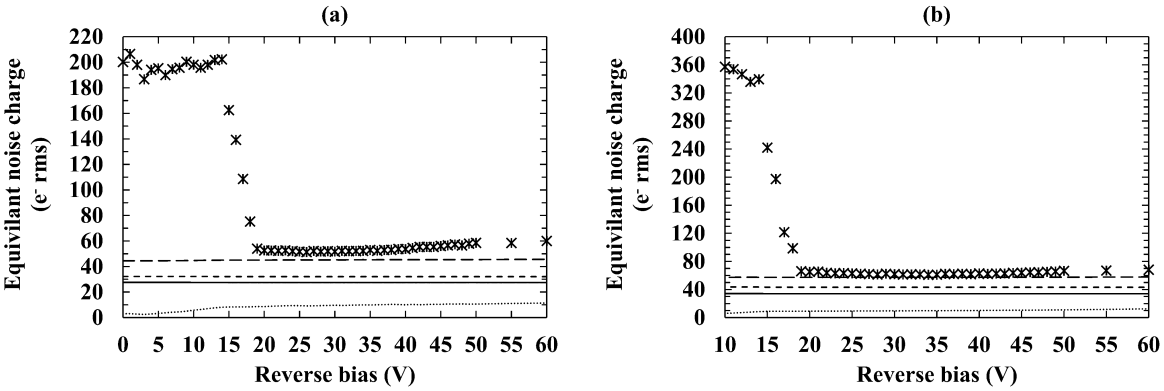

Fig. 15. Calculated noise contributions of the spectrometers (a) S_{200} and (b) S_{400} as a function of applied detector reverse bias at a shaping time of 0.5 µs, and at 20 ºC: total noise (stars); sum of the calculated noise contributions (long dashed line); known series white noise (short dashed line); known dielectric noise (solid line); calculated parallel white noise (dotted line).

As per Fig. 15, the total sum of the calculated noise contributions (Fano noise, 1/*f* noise, known series white noise, known dielectric noise, and parallel white noise, added in quadrature) did not account for the measured total noise (FWHM at 5.9 keV) of the 200 µm and 400 µm diameter detector based spectroscopic systems. At an applied detector reverse bias of 10 V, the total noise of each system was 198 e^- rms ± 5 e^- rms, and 357 e^- rms ± 5 e^- rms for S_{200} and S_{400}, respectively. At the same applied bias (10 V), the total sum of the calculated noise contributions was 44.7 e^- rms ± 0.4 e^- rms and 57.4 e^- rms ± 0.2 e^- rms, respectively. This discrepancy was attributed in part to incomplete charge collection noise, where charge carriers cannot readily travel through the $Al_{0.8}Ga_{0.2}As$ junction before the punch-through voltage [18] (see Section IV.A). Stray dielectric noise, stray series white noise, and any stray parallel white noise contributions, arising from the spectroscopic systems, would have also contributed to the measured total noise.

As the applied detector reverse bias was further increased (14 V < V_R < 19 V), the measured total noise (FWHM at 5.9 keV) of each spectrometer improved (reduced). At 19 V applied detector reverse bias, the total noise was 54.0 e^- rms ± 0.5 e^- rms and 66.0 e^- rms ± 0.6 e^- rms for the spectrometers S_{200} and S_{400}, respectively. The total sum of the calculated noise contributions, at the same applied detector reverse bias (19 V), was 45.0 e^- rms ± 0.4 e^- rms and 57.3 e^- rms ± 0.2 e^- rms for the spectrometers S_{200} and S_{400}, respectively. This, in part, indicated that incomplete charge collection noise reduced as the punch-through voltage (≈ 14 V) was exceeded.

At the optimal applied detector reverse bias for each spectrometer (26 V and 34 V for the spectrometers S_{200} and S_{400} respectively), the measured apparent noise was 51.4 e^- rms ± 0.5 e^- rms and 61.0 e^- rms ± 0.6 e^- rms for the spectrometers S_{200} and S_{400}, respectively. The total sum of the calculated noise contributions, at the same optimal applied detector reverse bias (26 V and 34 V for S_{200} and S_{400} respectively), was 45.1 e^- rms ± 0.4 e^- rms and 57.4 e^- rms ± 0.2 e^- rms for the spectrometers S_{200} and S_{400}, respectively. The apparent decrease in remaining noise contribution between 19 V and the optimal applied detector reverse bias of each spectrometer indicated a net benefit due to avalanche multiplication.

At the maximum applied detector reverse bias (60 V) an apparent noise of 60.1 e^- rms ± 0.5 e^- rms and 68.0 e^- rms ± 0.5 e^- rms was measured for S_{200} and S_{400}, respectively. The total sum of the calculated noise contributions at the same applied detector reverse bias (60 V), was 45.6 e^- rms ± 0.4 e^- rms and 57.9 e^- rms ± 0.2 e^- rms, respectively. The increased discrepancy between the measured apparent noise (FWHM at 5.9 keV) and the total sum of the calculated noise contributions may have arisen from a larger than expected parallel white noise at high biases or from increasing excess noise due to avalanche multiplication.

D. Improvements in energy resolution due to avalanche multiplication

In order to determine whether avalanche multiplication affected the energy resolution of the reported spectrometers, the measured energy resolution (FWHM at 5.9 keV) was compared to the expected non-avalanche energy resolution of each spectrometer.

The expected non-avalanche energy resolution was calculated by assuming incomplete charge collection noise became negligible at $V_R \geq 19$ V, avalanche multiplication was not present at $V_R \leq 19$ V, and any stray noises contributing to the remaining noise contribution (see Section IV.C) were independent of applied reverse bias. Given these assumptions, the remaining noise contribution at $V_R = 19$ V for both spectrometers represents the non-avalanche mode remaining noise contribution across the applied reverse bias range ($19 \text{ V} \leq V_R \leq 60$ V). The remaining noise contribution at $V_R = 19$ V was calculated to be 29.8 e^- rms ± 1.1 e^- rms and 32.8 e^- rms ± 1.6 e^- rms for S_{200} and S_{400}, respectively.

Adding in quadrature the remaining noise contribution at $V_R = 19$ V to the calculated known noise contributions at each investigated applied detector reverse bias yields the expected non-avalanche energy resolution as a function of applied reverse bias within the range $19 \text{ V} \leq V_R \leq 60$ V. The expected non-avalanche energy resolution, and measured avalanche energy resolution, at each applied reverse bias for the spectrometers S_{200} and S_{400}, can be seen in Fig. 16.

At an applied detector reverse bias of 26 V ($M = 1.1$), an expected non-avalanche energy resolution of 535 eV ± 7 eV FWHM at 5.9 keV was calculated for the spectrometer S_{200}. Given the same spectrometer and the same applied detector reverse bias (26 V), an energy resolution of 508 eV ± 5 eV was measured. As for the spectrometer S_{400}, at an applied detector reverse bias of 34 V ($M = 1.2$), an expected non-avalanche energy resolution of 653 eV ± 8 eV FWHM at 5.9 keV was calculated. At the same applied detector reverse bias (34 V), an energy resolution of 603 eV ± 6 eV was measured. As such, it can be concluded that a noticeable benefit from small avalanche multiplication gains ($M \leq 1.4$) was measured. This conclusion is further supported by recent results from non-avalanche GaAs p^+-i-n^+ photodiodes. Those photodiodes were of identical design to the devices reported here except that they did not have the AlGaAs avalanche layer [27]. At 20 ºC, energy resolutions of 690 eV and 730 eV FWHM at 5.9 keV were reported for the 200 µm and 400 µm GaAs p^+-i-n^+ photodiode, respectively [27]. Thus it has been demonstrated that the addition of an avalanche layer can lead to improvement of the energy resolution in X-ray photodiodes.

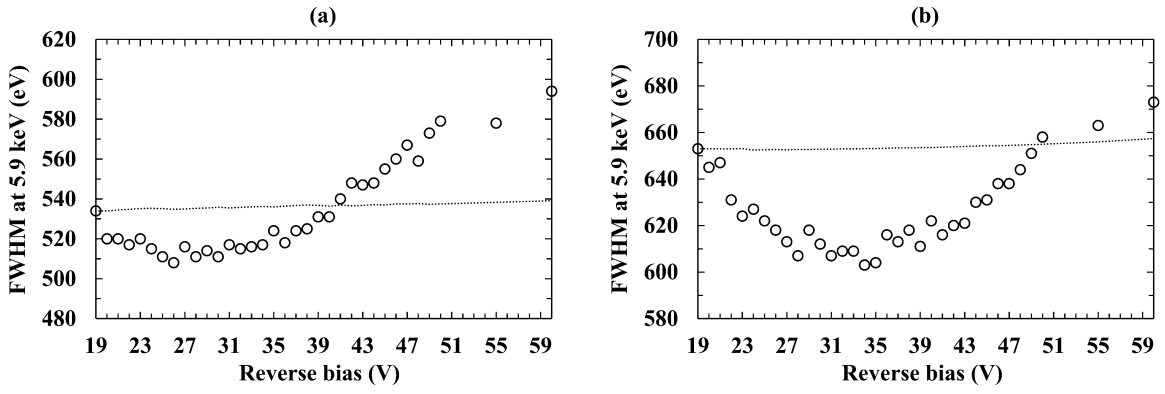

Fig. 16. Expected non-avalanche FWHM at 5.9 keV, assuming no incomplete charge collection noise at $V_R \geq 19$ V (dotted line), as a function of applied detector reverse bias to the spectrometers (a) S_{200} and (b) S_{400}. The measured FWHM at 5.9 keV (circles) has been included.

V. CONCLUSION

A 200 µm diameter and a 400 µm diameter, custom-made, circular GaAs/$Al_{0.8}Ga_{0.2}As$ separate absorption and multiplication (SAM) X-ray photodiode have each been characterised at room temperature (20 °C), and investigated for their response to ^{55}Fe X-rays (Mn Kα = 5.9 keV; Mn Kβ = 6.49 keV) source. Each device consisted of a 10 µm thick GaAs absorption layer and a 0.1 µm thick $Al_{0.8}Ga_{0.2}As$ multiplication layer.

Capacitance measurements indicated a punch-through voltage of ≈ 14 V for both devices. A capacitance of 1.12 pF and 2.20 pF (each ± 0.4 fF) was measured for the 200 µm and 400 µm diameter devices respectively at the maximum applied reverse bias (60 V). The capacitance measurements indicated that both devices were fully depleted at $V_R \geq 50$ V, reporting a depletion width consistent with growth specifications (see Table 1).

The best measured energy resolution achieved at 20 °C for the spectrometer S_{200} was 508 eV ± 5 eV FWHM at 5.9 keV, at an applied detector reverse bias of 26 V, corresponding to an apparent multiplication factor of 1.1. The best measured energy resolution at 20 °C for the spectrometer S_{400} was 603 eV ± 6 eV FWHM at 5.9 keV, at an applied detector reverse bias of 34 V, corresponding to an apparent multiplication factor of 1.2. Further increasing the applied detector reverse bias increased (worsened) the energy resolution (e.g. 594 eV ± 5 eV FWHM at 5.9 keV and 673 eV ± 5 eV FWHM at 5.9 keV for the spectrometers S_{200} and S_{400} respectively, at an applied detector reverse bias of 60 V). This indicated that any benefits from further increasing avalanche gain were exceeded by increases in excess noise and/or parallel white noise.

In order to determine whether avalanche multiplication affected the energy resolution of the spectrometers, the measured energy resolution (FWHM at 5.9 keV) was compared to the expected non-avalanche energy resolution of each spectrometer (see Section IV.D). The results indicated a noticeable benefit from small avalanche multiplication gains ($M \leq 1.4$). At an applied detector reverse bias of 26 V ($M = 1.1$), an expected non-avalanche energy resolution of 535 eV FWHM at 5.9 keV was calculated for the spectrometer S_{200}. Given the same spectrometer and the same applied detector reverse bias (26 V), an energy resolution of 508 eV FWHM at 5.9 keV was measured. Similarly, at an applied detector reverse bias of 34 V ($M = 1.2$), an expected non-avalanche energy resolution of 653 eV FWHM at 5.9 keV was calculated for the spectrometer S_{400}. Given the same spectrometer and the same applied detector reverse bias (34 V), an energy resolution of 603 eV FWHM at 5.9 keV was measured. The results were supported further (and set in context) by a recent study using non-avalanche GaAs p^+-i-n^+ photodiodes which did not have an AlGaAs avalanche layer [27]. At 20 ºC, energy resolutions of 690 eV and 730 eV FWHM at 5.9 keV were reported for the 200 µm and 400 µm GaAs p^+-i-n^+ photodiodes, respectively [27]. The results indicated that introducing a separate AlGaAs multiplication layer can be beneficial to GaAs photodiodes.

The energy resolution (FWHM at 5.9 keV) reported here is the best so far reported for GaAs/$Al_xGa_{1-x}As$ SAM APD X-ray spectrometers at room temperature. Energy resolutions of 1.08 keV FWHM at 5.9 keV [44] and 900 eV FWHM at 13.96 keV have been reported previously [18]. The measured energy resolution was also better than recently investigated non-avalanche $Al_xGa_{1-x}As$ detector based X-ray spectrometers, where an energy resolution of 760 eV FWHM at 5.9 keV was reported at room temperature [26]. However, the energy resolutions reported here are modest when compared to the best reported results for the best non-avalanche GaAs based X-ray

spectrometers (266 eV [3] and 300 eV [28] FWHM at 5.9 keV at room temperature) and the best Si based X-ray spectrometers (141 eV FWHM at 5.9 keV by [63] and 134 eV FWHM at 5.9 keV [64]), when those detectors are coupled to ultra-low-noise electronics better than those used for the investigations reported in the present article.

Despite the achieved energy resolutions of the presently reported GaAs/$Al_xGa_{1-x}As$ SAM APDs being not yet as good when compared to other more developed materials, X-ray spectrometers with modest energy resolutions can still provide important scientific contributions. For example, D-CIXS aboard SMART-1 [65] had an energy resolution of 420 eV FWHM at 4.5 keV [66] and measured, for the first time, Ti Kα (4.51 keV) X-ray fluorescence on the lunar surface [66]. An X-ray spectrometer with similar or slightly improved energy resolution, that is also radiation hard and temperature tolerant, could therefore find utility in future space science missions to harsh environments.

In future, the temperature dependence of the devices' electrical characteristics and X-ray detection performance will be studied. New SAM APDs will be fabricated in array format and characterised. Devices with thicker absorption regions will be grown to improve the quantum efficiency (thereby also reducing/eliminating the observed secondary photopeak as discussed in Section IV.B), and staircase avalanche regions implemented. A thicker absorption region would also reduce the detector capacitance, reducing the series white noise, and potentially improving the energy resolution of the spectrometer.

AUTHORS' DATA STATEMENT

The data that supports the findings of this study are available within the article [and its supplementary material].

ACKNOWLEDGEMENTS

This work was supported in part by Science and Technology Facilities Council, UK, Grants ST/P001815/1 and ST/M004635/1. M.D.C.W. acknowledges funding received from University of Sussex, UK, in the form of a PhD scholarship. A.M.B. acknowledges funding from the Leverhulme Trust, UK, in the form of a 2016 Philip Leverhulme Prize.

[1]P. Majewski, L. Andricek, A. Bahr, G. De Vita, B. Gunther, K. Hermenau, M. Hilchenbach, T. Lauf, P. Lechner, G. Lutz, D. Miessner, M. Porro, J. Reiffers, R. Richter, G. Schaller, M. Schnecke, F. Schopper, H. Soltau, A. Stefanescu, R. Strecker, L. Struder, and J. Treis, 2012, IEEE Transactions on Nuclear Science 59, 2479 (2012).

[2]D.N. Burrows, J.E. Hill, J.A. Nousek, J.A. Kennea, A. Wells, J.P. Osborne, A.F. Abbey, A. Beardmore, K. Mukerjee, A.D.T. Short, G. Chincarini, S. Campana, O. Citterio, A. Moretti, C. Pagani, G. Tagliaferri, P. Giommi, M. Capalbi, F. Tamburelli, L. Angelini, G. Cusumano, H.W. Bräuninger, W. Burkert, and G.G. Hartner, Space Science Reviews 120, 165 (2005).

[3]A. Owens, M. Bavdaz, A. Peacock, A. Poelaert, H. Andersson, S. Nenonen, H. Sipila, L. Tröger, and G. Bertuccio, Journal of Applied Physics 90, 5376 (2001).

[4]G. Bertuccio, R. Casiraghi, D. Maiocchi, A. Owens, M. Bavdaz, A. Peacock, H. Andersson, and S. Nenonen, IEEE Transactions on Nuclear Science 50, 723 (2003).

[5]A.M. Barnett, J.E. Lees, D.J. Bassford, J.S. Ng, C.H. Tan, N. Babazadeh, and R.B. Gomes, Nuclear Instruments and Methods in Physics Research Section A 654, 336 (2011).

[6]G. Lioliou, X. Meng, J.S. Ng, and A.M. Barnett, Journal of Applied Physics 119, 124507 (2016).

[7]A. Owens, M. Bavdaz, A. Peacock, A. Poelaert, H. Andersson, S. Nenonen, L. Tröger, and G. Bertuccio, Nuclear Instruments and Methods in Physics Research Section A 466, 168 (2001).

[8]H. Kagan, Nuclear Instruments and Methods in Physics Research Section A 546, 222 (2005).

[9]M. Zhang, B. Gu, L. Wang, and Y. Xia, Physics Letters A 332, 320 (2004).

[10]G. Bertuccio, and R. Casiraghi, IEEE Transactions on Nuclear Science 50, 175 (2003).

[11]G. Bertuccio, S. Caccia, D. Puglisi, and D. Macera, Nuclear Instruments and Methods in Physics Research Section A 652, 193 (2011).

[12]S. Zhao, T. Gohil, G. Lioliou, and A.M. Barnett, Nuclear Instruments and Methods in Physics Research Section A 830, 1 (2016).

[13]S. Butera, G. Lioliou, A.B. Krysa, and A.M. Barnett, Scientific Reports 7, 10206 (2017).

[14]G. Lioliou, A.B. Krysa, and A.M. Barnett, Journal of Applied Physics 124, 195704 (2018).

[15]A. Auckloo, J.S. Cheong, X. Meng, C.H. Tan, J.S. Ng, A.B. Krysa, R.C. Tozer, and J.P.R. David, Journal of Instrumentation 11, P03021 (2016).

[16]S. Butera, G. Lioliou, A.B. Krysa, and A.M. Barnett, Journal of Applied Physics 120, 024502 (2016).

[17]S. Butera, T. Gohil, G. Lioliou, A.B. Krysa, and A.M. Barnett, Journal of Applied Physics 120, 174503 (2016).

[18]J. Lauter, D. Protić, A. Förster, and H. Lüth, Nuclear Instruments and Methods in Physics Research Section A 356, 324 (1995).

[19]A.M. Barnett, G. Lioliou, and J.S. Ng, Nuclear Instruments and Methods in Physics Research Section A 774, 29 (2015).

[20]A. Silenas, J. Pozela, K. Pozela, L. Dapkus, and V. Juciene, Nuclear Instruments and Methods in Physics Research Section A 563, 21 (2006).

[21]M.D.C. Whitaker, S. Butera, G. Lioliou, and A.M. Barnett, Journal of Applied Physics 122, 034501 (2017).

[22]A. Owens, and A. Peacock, Nuclear Instruments and Methods in Physics Research Section A 531, 18 (2004).

[23]B.L. Henke, E.M. Gullikson, and J.C. Davis, Atomic Data and Nuclear Data Tables 54, 181 (1993).

[24]G.P. Summers, E.A. Burke, P. Shapiro, S.R. Messenger, and R.J. Walters, IEEE Transactions on Nuclear Science 40, 1372 (1993).

[25]G. Lioliou, and A.M. Barnett, Nuclear Instruments and Methods in Physics Research Section A 801, 63 (2015).

[26]M.D.C. Whitaker, G. Lioliou, and A.M. Barnett, Nuclear Instruments and Methods in Physics Research Section A 899, 106 (2018).

[27]G. Lioliou, M.D.C. Whitaker, and A.M. Barnett, Journal of Applied Physics 122, 244506 (2017).

[28]C. Erd, A. Owens, G. Brammertz, M. Bavdaz, A. Peacock, V. Lämsä, S. Nenonen, H. Andersson, and N. Haack, Nuclear Instruments and Methods in Physics Research Section A 487, 78 (2002).

[29]A.M. Barnett, D.J. Bassford, J.E. Lees, J.S. Ng, C.H. Tan, and J.P.R. David, Nuclear Instruments and Methods in Physics Research Section A 621, 453 (2010).

[30]J.C. Campbell, Journal of Lightwave Technology 25, 109 (2007).

[31]J.P.R. David, and C.H. Tan, IEEE Journal of Selected Topics in Quantum Electronics 14, 998 (2008).

[32]J. Kou1, K. Tian, C. Chu, Y. Zhang, X. Zhou, Z. Feng, and Z. Zhang, Nanoscale Research Letters 14, 396 (2019).

[33]X. Zhou, X. Tan, Y. Lv, Y. Wang, J. Li, T. Han, H. Guo, S. Liang, Z. Zhang, Z. Feng, and S. Cai, IEEE Electron Device Letters 40, 1591 (2019).

[34]S.M. Sze, *Physics of Semiconductor Devices*, 3rd ed. (John Wiley & Sons, New Jersey, 2007).

[35]A.M. Barnett, J.E. Lees, D.J. Bassford, J.S. Ng, C.H. Tan, and R.B. Gomez, Nuclear Instruments and Methods in Physics Research Section A 626, 25 (2011).

[36]C.H. Tan, J.P.R. David, S.A. Plimmer, G.J. Rees, R.C. Tozer, and R. Grey, IEEE Transactions on Electron Devices 48, 1310 (2001).

[37]R.J. McIntyre, IEEE Transactions on Electron Devices 13, 164 (1966).

[38]C.H. Tan, R.B. Gomes, J.P.R. David, A.M. Barnett, D.J. Bassford, J.E. Lees, and J.S. Ng, IEEE Transactions on Electron Devices 58, 1696 (2011).

[39]G.W. Fraser, *X-ray Detectors in Astronomy* (Cambridge University Press, Cambridge, 2016).

[40]J. David, 2016, Nature Photonics 10, 364 (2016).

[41]F. Capasso, T. Won-Tien, and G.F. Williams, IEEE Transactions on Electron Devices 30, 381 (1983).

[42]G. Ripamonti, F. Capasso, A.L. Hutchinson, D.J. Muehlner, J.F. Walker, and R.J. Malik, Nuclear Instruments and Methods in Physics Research Section A 288, 99 (1990).

[43]C.K. Chia, B.K. Ng, J.P.R. David, G.J. Rees, R.C. Tozer, M. Hopkinson, R.J. Airey, and P.N. Robson, Journal of Applied Physics 94, 2631 (2003).

[44]R.B. Gomes, C.H. Tan, X. Meng, J.P.R. David, and J.S. Ng, Journal of Instrumentation 9, P03014 (2014).

[45]S. Butera, M.D.C. Whitaker, G. Lioliou, and A.M. Barnett, Scientific Reports 6, 38409 (2016).

[46]M.R. Brozel, and G.E. Stillman, *Properties of Gallium Arsenide*, 3rd ed. (The Institution of Electrical Engineers, London, 1996).

[47]S. Adachi, *Properties of aluminium gallium arsenide*, EMIS Datareviews Series No. 7 INSPEC (The Institution of Electrical Engineers, London, 1993).

[48]R.A. Stradling, and P.C. Klipstein, *Growth and characterisation of semiconductors*, 1st ed. (IOP Publishing Ltd, Bristol, 1991).

[49]G. Lioliou, *Wide Bandgap Semiconductor Radiation Detectors for Extreme Environments*, PhD Thesis (Department of Engineering and Informatics, University of Sussex, Sussex, 2017).

[50]M. Takenaka, K. Morii, M. Sugiyama, Y. Nakano, and S. Takagi, Optics Express 20, 8718 (2012).

[51]G. Bertuccio, P. Rehak, and D. Xi, Nuclear Instruments and Methods in Physics Research Section A 326, 71 (1993).

[52]A.M. Barnett, J.E. Lees, and D.J. Bassford, Journal of Instrumentation 8, 1 (2013).

[53]U. Schötzig, Applied Radiation and Isotopes 53, 469 (2000).

[54]G. Bertuccio, and D. Maiocchi, Journal of Applied Physics 92, 1248 (2002).

[55]A.M. Barnett, J.E. Lees, and D.J. Bassford, Applied Physics Letters 102, 181119 (2013).

[56]G. Bertuccio, IEEE Solid State Circuits Magazine 4, 36 (2012).

[57]G. Lioliou, and A.M. Barnett, Nuclear Instruments and Methods in Physics Research Section A 801, 63 (2015).

[58]G. Bertuccio, A. Pullia, J. Lauter, A. Forster, and H. Luth, IEEE Transactions on Nuclear Science 44, 1 (1997).

[59]G. Bertuccio, A. Pullia, and G. De Geronimo, Nuclear Instruments and Methods in Physics Research Section A 380, 301 (1996).

[60]Siliconix, *2N4416/2N4416A/SST4416 N-Channel JFETs*, Data Sheet, 70242 S-04028, Rev. F, 04-Jun-01 (Vishay Electronic GmbH, Selb, 2001).

[61]A.M. Barnett, J.E. Lees, D.J. Bassford, and J.S. Ng, Nuclear Instruments and Methods in Physics Research Section A 673, 10 (2012).

[62]G. Bertuccio, and A. Pullia, 1993, Review of Scientific Instruments 64, 3294 (1993).

[63]G. Bertuccio, M. Ahangarianabhari, C. Graziani, D. Macera, Y. Shi, A. Rachevski, I. Rashevskaya, A. Vacchi, G. Zampa, N. Zampa, P. Bellutti, G. Giacomini, A. Picciotto, and C. Piemonte, 2015, *A Silicon Drift Detector-CMOS front-end system for high resolution X-ray spectroscopy up to room temperature*, Journal of Instrumentation 10, P01002 (2015).

[64]J. Müller-Seidlitz, R. Andritschke, A. Bähr, N. Meidinger, S. Ott, R.H. Richter, W. Treberspurg, and J. Treis, *Spectroscopic performance of DEPFET active pixel sensor prototypes suitable for the high count rate Athena WFI detector* (SPIE Astronomical Telescopes + Instrumentation, Edinburgh, 2016).

[65]M. Grande, R. Browning, N. Waltham, D. Parker, S.K. Dunkin, B. Kent, B. Kellett, C.H. Perry, B. Swinyard, A. Perry, J. Feraday, C. Howe, G. Mcbride, K. Phillips, J. Huovelin, P. Muhli, P.J. Hakala, O. Vilhu, J. Laukkanen, N. Thomas, D. Hughes, H. Alleyne, M. Grady, R. Lundin, S. Barabash, D. Baker, P.E. Clark, C.D. Murray, J. Guest, I. Casanova, L.C. D'uston, S. Maurice, B. Foing, D.J. Heather, V. Fernandes, K. Muinonen, S.S. Russell,

741 A. Christou, C. Owen, P. Charles, H. Koskinen, M. Kato, K. Sipila, S. Nenonen, M. Holmstrom, N. Bhandari, R.
742 Elphic, and D. Lawrence, Planetary and Space Science 51, 427 (2003).
743
744 [66]B.M. Swinyard, K.H. Joy, B.J. Kellett, I.A. Crawford, M. Grande, C.J. Howe, V.A. Fernandes, O. Gasnault, D.J.
745 Lawrence, S.S. Russell, M.A. Wieczorek, and B.H. Foing, Planetary and Space Science 57, 744 (2009).